SUPER-RESOLUTION USING FLOW ESTIMATION IN CONTRAST ENHANCED ULTRASOUND IMAGING

Oren Solomon[⋆] *Ruud JG van Sloun*[†] *Massimo Mischi*[†] *Yonina C. Eldar*[⋆]

[⋆]Department of Electrical Engineering, Technion, Haifa 32000, Israel,
[†]Department of Electrical Engineering, Eindhoven University of Technology, The Netherlands.

ABSTRACT

Ultrasound localization microscopy offers new radiation-free diagnostic tools for vascular imaging deep within the tissue. Despite its high spatial resolution, low microbubble concentrations dictate the acquisition of tens of thousands of images, over the course of several seconds to tens of seconds, to produce a single super-resolved image. To address this limitation, sparsity-based approaches have recently been proposed to significantly reduce the total acquisition time, by resolving the vasculature in settings with considerable microbubble overlap. Here, we report on initial results of improving the spatial resolution and visual vascular reconstruction quality of sparsity-based super-resolution ultrasound imaging from low frame-rate acquisitions, by exploiting the inherent kinematics of microbubbles' flow. Our method relies on simultaneous tracking and sparsity-based detection of individual microbubbles.

Index Terms— Ultrasound, Contrast agents, Super-resolution, Compressed sensing, Kalman filter.

I. INTRODUCTION

In recent years, super-resolution contrast-enhanced ultrasound (US) imaging has emerged, and enabled a fine visualization and detailed assessment of capillary blood vessels *in vivo* [1–7]. Super-resolution US relies on concepts borrowed from super-resolution fluorescence microscopy techniques such as photo-activated localization microscopy (PALM) [8]. Similarly, in contrast enhanced US (CEUS) individual resonating microbubbles (MBs) are injected into the bloodstream, as means to image blood vessels with improved contrast. They are similar in size to red blood cells, thus can be regarded as point emitters. Their subsequent localizations are also accumulated, producing a final super-resolved image of the vascular bed with a ten-fold improved spatial resolution compared with standard CEUS imaging. To obtain reliable localizations, low MB concentrations are typically used [2, 3]. Despite yielding a substantial improvement in spatial resolution and blood velocity measurements in sub-diffraction vessels, super-resolution ultrasound imaging typically requires tens of thousands of frames to produce a single super-resolved image.

This research was supported by the I-CORE program of the planning and budgeting committee and the Israel science foundation (1802/12).

To overcome the temporal limitation of localization-based super-resolution without compromising the spatial resolution of the reconstructed image, sparsity-based [9] approaches were recently proposed [10–13], as well as a deep-learning based approach [14]. These techniques favor high-density acquisitions with overlapping MBs to reduce the total imaging time. In [10, 15], sparsity-based super-resolution US hemodynamic imaging (SUSHI), using ultrafast plane-wave acquisition, demonstrated a super-resolved time-lapse movie of 25Hz, showing super-resolved hemodynamic changes in blood flow within a rabbit's kidney. In [12], using a clinically approved scanner with an acquisition rate of 10Hz, a super-resolved image of a human prostate vasculature was obtained, by performing frame-by-frame sparse localization. However, no information about blood flow characteristics was recovered in these methods.

Moreover, while previous super-resolution works focused on ultrafast plane-wave image acquisition, e.g. [1, 13, 15], most clinically used scanners are low-rate scanners (10-25Hz). When using high frame-rate scanners, e.g. ultrafast plane-wave imaging, fast super-resolution imaging can be achieved via SUSHI [10, 13, 15]. However, as the frame-rate decreases, MB detections become more sporadic, resulting in inconsistent depiction of the vessels. Thus, the so-called missing information needs to be filled-in by other means, albeit with higher computational cost.

Here we improve upon sparsity-based super-resolution CEUS imaging, by exploiting the inherent flow of MBs as an additional structural prior to achieve super-resolution from images obtained by low frame-rate US scanners. Our method, termed simultaneous sparsity-based super-resolution and tracking, or 3SAT, combines weighted sparse recovery with simultaneous tracking of the individual MBs in the imaging plane. The structural movement of MBs in the bloodstream dictates that MBs are more likely to be found in certain areas of the next frame, given their past and current locations. The position history of each MB is used to estimate the position of the MBs in the next frame, which in turn is used to form a weighting matrix for weighted sparse recovery for locating the MBs. This allows to favor

more likely locations in the sparse recovery process. With the addition of each new frame, the tracks are updated online. Since our approach tracks individual MBs, it is possible to also estimate their velocities.

The reconstruction process of 3SAT can be considered as sparse recovery with time-varying support [16–19], where the support represents the MB locations. 3SAT differs from these methods in the following manner. First, previous works assume a first-order recursion for the propagation model of the non-zero entries of the sparse signals In this case, only the support of the sparse signal is of interest, but in CEUS, MB kinematics also include varying velocities. Here, an extended model is considered, which includes the position estimation of the MBs together with their velocities. Second, as MBs flow over time, new MBs appear and some MBs vanish from the imaging plane, due to the 3D geometry of the blood vessels. It is thus desirable to associate new MBs to previous localizations to improve the overall tracking and to achieve a more reliable estimation of their motion kinematics. This association process is not considered in prior works on sparse recovery with time-varying support, but is taken into account in 3SAT by the use of an automatic association algorithm, combined with Kalman filtering.

The rest of the paper is organized as follows. Section II describes 3SAT and each of its building blocks. Section III presents simulation results. Conclusions are presented in Section IV.

Throughout the paper, x represents a scalar, $\mathbf{x}$ a vector, $\mathbf{X}$ a matrix and $\mathbf{I}_{N\times N}$ is the $N \times N$ identity matrix. The notation $\mathbf{X}^T$ represents the transpose of $\mathbf{X}$ and $\mathbf{X}^H$ its conjugate transpose. The notation $||\cdot||_p$ represents the standard p-norm and $||\cdot||_F$ is the Frobenius norm. Subscript x_l denotes the lth element of $\mathbf{x}$ and $\mathbf{x}_l$ is the lth column of $\mathbf{X}$, while superscript $(\cdot)^p$ refers to the pth MB. The estimated vector in frame k, given the estimate in the $(k-1)$th frame, is indicated by $\mathbf{s}_{k|k-1}$. Likewise $\mathbf{P}_{k|k-1}$ indicates its estimated covariance matrix k, given the $k-1$ estimate. The ijth element of a matrix $\mathbf{A}$ is denoted $A[i,j]$.

II. SIMULTANEOUS SPARSITY-BASED SUPER-RESOLUTION AND TRACKING

II-A. Weighted sparse recovery

We start from a contrast-enhanced ultrasound sequence of K frames where each frame consists of $M \times M$ pixels. Prior to 3SAT processing, all frames are registered, as described in [12]. Similar to [11], a frame is modeled as a summation of L_k individual MB echoes,

$$Z_k(x,y) = \sum_{i=1}^{L_k} u(x-x_i, y-y_i)\sigma_i, \tag{1}$$

where $u(\cdot,\cdot)$ is the point spread function (PSF) of the transducer and σ_i is the magnitude of the returned echo from the ith MB located at position (x_i, y_i). The PSF of the transducer is assumed to be known.

Following similar derivations to [15], we discretize the kth frame in (1) as $\mathbf{Z}_k, k = 1,\ldots,K$ of size $M \times M$, and denote its vectorized form $\mathbf{z}_k$. We also introduce a high-resolution grid of size $N \times N$ pixels, such that $N = PM$ for some $P \geq 1$ and denote the (vectorized) super-resolved frame k, which contains the locations of the MBs on the high-resolution grid, by $\mathbf{i}_k$. Using knowledge of the PSF, the measured frame $\mathbf{z}_k$ is related to the super-resolved frame $\mathbf{i}_k$ via

$$\mathbf{z}_k = \mathbf{H}\mathbf{i}_k, \tag{2}$$

where $\mathbf{H}$ is a known matrix, based on the PSF. Estimation of $\mathbf{i}_k$ is achieved by solving the following convex optimization problem,

$$\min_{\mathbf{i}_k \geq \mathbf{0}} ||\mathbf{z}_k - \mathbf{H}\mathbf{i}_k||_2^2 + \lambda||\mathbf{i}_k||_1, \tag{3}$$

where $\lambda \geq 0$ is a regularization parameter.

In [12], the super-resolved image is constructed by solving (3) for each frame k and accumulating all localizations. To improve the sparse recovery process, we propose solving the following weighted l_1 minimization problem,

$$\min_{\mathbf{i_k} \geq \mathbf{0}} ||\mathbf{z}_k - \mathbf{H}\mathbf{i}_k||_2^2 + \lambda||\mathbf{W}_k\mathbf{i}_k||_1. \tag{4}$$

The matrix $\mathbf{W}_k$ is an $N^2 \times N^2$ diagonal weights matrix which incorporates the flow dynamics of the MBs in the sparse recovery process, and changes with each frame. Intuitively, this matrix assigns higher weights (penalty) to locations less probable to contain MBs, thus forcing the sparse recovery process to favor specific locations in the frame, which are more likely to contain the MBs. In practice, (4) is minimized using the FISTA algorithm [20, 21], or by using the reweighted iterative l_1 method [22].

II-B. Microbubble tracking

The (diagonal of the) weighting matrix $\mathbf{W}_k$ is inversely proportional to the accumulated probability of detected MBs from the $(k-1)$th frame to be found in new locations in the kth frame. Its construction requires identifying and tracking individual MBs. First, the state of the pth MB in frame k is defined as $\mathbf{s}_k^p \in \mathbb{R}^4$ with

$$\mathbf{s}_k^p = [x_k^p, v_{x_k}^{\ p}, y_k^p, v_{y_k}^{\ p}]^T.$$

Here, x_k^p and y_k^p are Cartesian coordinates which indicate the position of the pth MB in frame k, and $v_{x_k}^{\ p}$ and $v_{y_k}^{\ p}$ its respective velocity components. The accumulation of all states of the pth MB from frame 1 to frame K_p, $\mathbf{T}^p = [\mathbf{s}_1^p, \ldots, \mathbf{s}_{K_p}^p] \in \mathbb{R}^{4\times K_p}$, is referred to as the track of the pth MB.

To proceed, consider an arbitrary frame, k. At this stage, we posses all the states of P_{k-1} previously tracked MBs, $\mathbf{s}_{k-1}^1, \ldots, \mathbf{s}_{k-1}^{P_{k-1}}$. Given the next low-resolution frame $\mathbf{z}_k$, our main two goals are:

1) Recover the locations of the L_k MBs which are embodied in frame $\mathbf{z}_k$. The number L_k of MBs in frame k is generally different than the number of MBs in the previous frame L_{k-1}.
2) Associate each newly detected MB to a previously known track, or open a new track if no such association is possible.

Denote the $(k-1)$th super-resolved frame as $\mathbf{i}_{k-1}$ (by minimizing (4)), whose non-zero values correspond to the positions of the MBs present in this frame. Next, given all previously known tracks $\mathbf{T}^1, \ldots, \mathbf{T}^{P_{k-1}}$, these positions need to be associated to the tracks. The updated tracks are essential to the formulation of $\mathbf{W}_k$. Specifically, this matching and association process is realized using the multiple hypothesis tracking (MHT) procedure [23, 24]. The MHT algorithm, as first suggested by Reid, is considered as one of the most popular and well known data association techniques.

Track update and propagation is performed by applying Kalman filtering to each track. Individual tracks represent the history of each detected MB. This history helps propagate the MBs to the next frame more accurately, and to obtain improved velocity estimation. To this end, consider the pth track. We assume a linear propagation model for the locations of the individual MBs between consecutive frames, given by

$$\mathbf{s}_k^p = \mathbf{\Phi}\mathbf{s}_{k-1}^p + \boldsymbol{\eta}_k^p, \quad \mathbf{\Phi} = \begin{bmatrix} 1 & \Delta T & 0 & 0 \\ 0 & 1 & 0 & 0 \\ 0 & 0 & 1 & \Delta T \\ 0 & 0 & 0 & 1 \end{bmatrix}, \quad (5)$$

with $1/\Delta T$ being the frame-rate of the US machine. Model (5) corresponds to the discretized version of the *continuous white noise acceleration (CWNA) model*, or *second-order kinematic model* [25]. Ideally, a constant velocity model has zero acceleration, or zero second-order derivative. In practice, CWNA assumes that the velocity of each MB has slight perturbations, described by zero-mean white noise with power spectral density ρ. In (5), this uncertainty is captured by the zero-mean additive Gaussian noise vector $\boldsymbol{\eta}_k^p$, associated with a covariance matrix $E\{\boldsymbol{\eta}_k^p \boldsymbol{\eta}_k^{p^T}\} = \mathbf{Q}_k^p$. Following [25], the CWNA covariance matrix $\mathbf{Q}_k^p$ is given by

$$\mathbf{Q}_k^p = \begin{bmatrix} 1/3\Delta T^3 & 1/2\Delta T^2 & 0 & 0 \\ 1/2\Delta T^2 & \Delta T & 0 & 0 \\ 0 & 0 & 1/3\Delta T^3 & 1/2\Delta T^2 \\ 0 & 0 & 1/2\Delta T^2 & \Delta T \end{bmatrix} \rho,$$

where ρ is chosen empirically.

The measurement model for the pth MB is then given by

$$\mathbf{y}_k^p = \mathbf{s}_{k-1}^p + \boldsymbol{\zeta}_k^p, \quad (6)$$

were $\boldsymbol{\zeta}_k^p$ is zero-mean independent i.i.d. Gaussian noise with covariance matrix $E\{\boldsymbol{\zeta}_k^p \boldsymbol{\zeta}_k^{p^T}\} = \mathbf{R}_k^p$. In practice, this matrix is chosen to be diagonal.

From the super-resolved image $\mathbf{i}_{k-1}$ we measure the position of the MBs. Specifically, consider a MB which is detected in position $[n_k\Delta_X, n_y\Delta_Y]$, where Δ_X and Δ_Y are the known sizes of each pixel in the super-resolved image and $[n_k, n_y]$ are some integers. If the MHT algorithm associated this MB to the pth track, then $y_k^p[1] = n_k\Delta_X$ and $y_k^p[3] = n_k\Delta_Y$. Rough velocity measurements of the MBs, or $y_k^p[2]$ and $y_k^p[4]$, are measured using optical flow (OF) estimation [26] on the low-resolution movie frames, to provide additional information for the Kalman filter.

Given the propagation (5) and the measurement (6) models, the Kalman filter update rules are now formulated. MB state propagation to the next frame and its corresponding propagated estimation covariance matrix are given by

$$\begin{aligned} \mathbf{s}_{k|k-1}^p &= \mathbf{\Phi}\mathbf{s}_{k-1|k-1}^p, \\ \mathbf{P}_{k|k-1}^p &= \mathbf{\Phi}\mathbf{P}_{k-1|k-1}^p\mathbf{\Phi}^T + \mathbf{Q}_k^p. \end{aligned} \quad (7)$$

Using (7), the weighting matrix $\mathbf{W}_k$ is calculated as described in Section II-C. Next, (4) is minimized to recover the kth super-resolved frame, $\mathbf{i}_k$. After the association process is finished, for each track we update its last state via the Kalman filter equations. The Kalman gain is given by

$$\mathbf{K}_k^p = \mathbf{P}_{k|k-1}^p(\mathbf{P}_{k|k-1}^p + \mathbf{R}_k^p)^{-1}, \quad (8)$$

and the innovation step along with the updated estimation error covariance matrix are

$$\begin{aligned} \mathbf{s}_{k|k}^p &= \mathbf{s}_{k|k-1}^p + \mathbf{K}_k^p(\mathbf{y}_k^p - \mathbf{s}_{k|k-1}^p) \\ \mathbf{P}_{k|k}^p &= (\mathbf{I}_{4\times4} - \mathbf{K}_k^p)\mathbf{P}_{k|k-1}^p. \end{aligned} \quad (9)$$

From the innovation step (9), the states are updated as $\mathbf{s}_k^p = \mathbf{s}_{k|k}^p$ with estimation covariance matrix $\mathbf{P}_k^p = \mathbf{P}_{k|k}^p$.

II-C. Weighting matrix formulation

After the states for all MBs are propagated using (7) and associated to existing or new tracks, we turn to formulate the weighting matrix $\mathbf{W}_k$. The propagated state $\mathbf{s}_{k|k-1}^p$ represents the position and velocity of the pth MB, and has its associated estimation error covariance matrix $\mathbf{P}_{k|k-1}^p$. Based on state predictions, a spatial MB-likelihood map $\mathbf{J}_k$ is formulated, by assigning probabilities drawn from an anisotropic Gaussian distribution of which the mean and covariance are dictated by their respective predictions/updates in the Kalman framework.

By aggregating the estimated positions and Gaussians of all of the P_{k-1} propagated MBs, a spatial map of their possible true locations on the high-resolution grid is constructed, denoted as $\mathbf{J}_k$. The ijth element of this $N \times N$ matrix is expressed as

$$\begin{aligned} &J_k[i,j] \\ &= \sum_{p=1}^{P_{k-1}} A^p e^{-q^p\left(\frac{1}{\sigma_x^{p2}}(i-x_0^p)^2 - c^p(i-x_0^p)(j-y_0^p) + \frac{1}{\sigma_y^{p2}}(j-y_0^p)^2\right)}, \end{aligned} \quad (10)$$

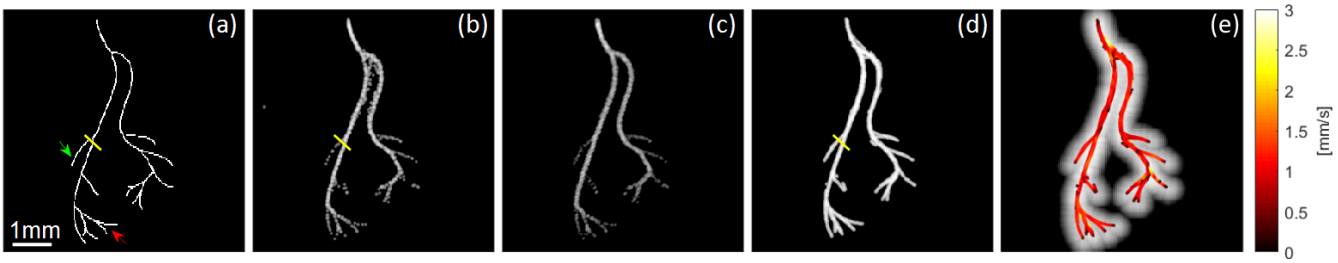

Fig. 1. Simulation results. (a) Ground truth image of bifurcating blood vessels. (b) Super-localization reconstruction, implemented by ThunderSTORM [27]. (c) Super-resolution sparse recovery obtained by minimizing (3) via FISTA. (d) 3SAT recovery, by accumulating all recovered MB trajectories. (e) Superimposed velocity trajectories over the maximum intensity projection (MIP) image, obtained from the 3SAT recovery. Yellow lines indicate selected profiles, presented in Fig. 2. All reconstructions are displayed in logarithmic scale, with a dynamic range of 40dB.

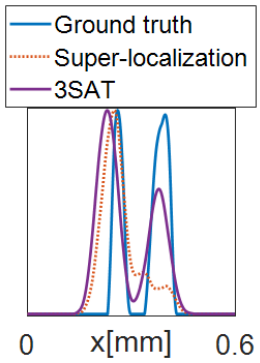

Fig. 2. Intensity profiles (a. u.) taken along the yellow lines in panels (a), (b) and (d) of Fig. 1. Peak to peak distance in the ground truth profile is 150 μm.

with $A^p = \sqrt{|2\pi \mathbf{P}^p_{k|k-1}|}$, $[x^p_0, y^p_0] = [s^p_{k|k-1}[1], s^p_{k|k-1}[3]]$, $\sigma^p_x = P^p_{k|k-1}[1,1]$, $\sigma^p_y = P^p_{k|k-1}[3,3]$, $q^p = 1/(2(1-\rho^{p2}))$, $c^p = 2\rho^p/(\sigma^p_x \sigma^p_y)$ and $\rho^p = P^p_{k|k-1}[1,3]/(\sigma^p_x \sigma^p_y)$. The diagonal of the weighting matrix $\mathbf{W}_k$ is the inverse of the vectorized form of $\mathbf{J}_k$ plus a regularization value ϵ, to avoid division by zero,

$$W_k[i,i] = \frac{1}{J_k[\lfloor i/N \rfloor, (i \mod N)] + \epsilon}, \quad i = 1, \ldots, N^2, \tag{11}$$

where $\lfloor \cdot \rfloor$ is the floor operation and $(x \mod y)$ is the modulo operation with the swap $0 \rightarrow N$. Vectorization of this $N \times N$ image is the diagonal of $\mathbf{W}_k$.

III. RESULTS

Figure 1 shows reconstruction results of the simulated dataset of flowing MBs within a simulated vascular network. Visual inspection reveals that 3SAT recovery (panel (d)) seems the smoothest and most continuous, depicting a more complete image of the vascular network, compared with standard (centroid-based) super-localization (panel (b)). The latter is a very discontinuous reconstruction, especially at the peripheral vessels. Sparsity-based reconstruction, which does not exploit MB kinematics and depicted in panel (c), seems more smooth and consistent than super-localization, but not all the vessels are connected, as presented in panel (d). The green arrow in panel (a) indicates a bifurcating blood vessel, which is almost non-depicted in the super-localization image (panel (b)), and is discontinuous in panel (c) of the sparsity-driven approach. In contrast, 3SAT (panel (d)) detects this blood vessel completely, showing a continuous connection to the main blood vessel. The red arrow indicates blood vessel branching which can also be observed in all three approaches. Panel (e) demonstrates the ability of 3SAT to simultaneously estimate velocities, which are in the range of $0 - 3$mm/s.

In Fig. 2, selected intensity profiles (a. u.) were measured along the solid yellow lines in panels (a), (b) and (d) of Fig. 1. In this example, it is evident that the 3SAT profile reveals the two peaks (vessel branching) also present in the ground truth, while the standard super-localization procedure fails to detect the rightmost peak.

IV. CONCLUSIONS

In this work, we aim to improve super-resolution imaging of low frame-rate US scanners, by reporting on initial results of a new algorithm to improve sparsity-based super-resolution. By formulating a weighted sparse recovery minimization problem, combined with on-line tracking of individual MBs, we are able to improve the sparse recovery process. 3SAT achieves a smoother depiction of the vasculature and provides quantitative information regarding MB kinematics.

REFERENCES

[1] C. Errico, J. Pierre, S. Pezet, Y. Desailly, Z. Lenkei, O. Couture, and M. Tanter, "Ultrafast ultrasound localization microscopy for deep super-resolution vascular imaging," *Nature*, vol. 527, no. 7579, pp. 499–502, 2015.

[2] M. A. OReilly and K. Hynynen, "A super-resolution ultrasound method for brain vascular mapping," *Medical physics*, vol. 40, no. 11, 2013.

[3] K. Christensen-Jeffries, R. J. Browning, M.-X. Tang, C. Dunsby, and R. J. Eckersley, "In vivo acoustic super-resolution and super-resolved

velocity mapping using microbubbles," *IEEE transactions on medical imaging*, vol. 34, no. 2, pp. 433–440, 2015.
[4] D. Ackermann and G. Schmitz, "Detection and tracking of multiple microbubbles in ultrasound B-mode images," *IEEE transactions on ultrasonics, ferroelectrics, and frequency control*, vol. 63, no. 1, pp. 72–82, 2016.
[5] T. Opacic, S. Dencks, B. Theek, M. Piepenbrock, D. Ackermann, A. Rix, T. Lammers, E. Stickeler, S. Delorme, G. Schmitz *et al.*, "Motion model ultrasound localization microscopy for preclinical and clinical multiparametric tumor characterization," *Nature communications*, vol. 9, no. 1, p. 1527, 2018.
[6] J. Foiret, H. Zhang, T. Ilovitsh, L. Mahakian, S. Tam, and K. W. Ferrara, "Ultrasound localization microscopy to image and assess microvasculature in a rat kidney," *Scientific reports*, vol. 7, no. 1, p. 13662, 2017.
[7] A. Bar-Zion, C. Tremblay-Darveau, O. Solomon, D. Adam, and Y. C. Eldar, "Fast vascular ultrasound imaging with enhanced spatial resolution and background rejection," *IEEE transactions on medical imaging*, vol. 36, no. 1, pp. 169–180, 2017.
[8] E. Betzig, G. H. Patterson, R. Sougrat, O. W. Lindwasser, S. Olenych, J. S. Bonifacino, M. W. Davidson, J. Lippincott-Schwartz, and H. F. Hess, "Imaging intracellular fluorescent proteins at nanometer resolution." *Science (New York, N.Y.)*, vol. 313, no. 5793, pp. 1642–1645, 2006.
[9] Y. C. Eldar, *Sampling Theory: Beyond Bandlimited Systems*. Cambridge University Press, 2015.
[10] O. Solomon, A. Bar-Zion, D. Adam, and Y. C. Eldar, "Fast and background free super-resolution ultrasound angiography," in *Ultrasonics Symposium (IUS), 2017 IEEE International*. IEEE, 2017, pp. 1–1.
[11] A. Bar-Zion, O. Solomon, C. Tremblay-Darveau, D. Adam, and Y. C. Eldar, "SUSHI: Sparsity-based ultrasound super-resolution hemodynamic imaging," *IEEE transactions on ultrasonics, ferroelectrics, and frequency control*, vol. 65, no. 12, pp. 2365–2380, 2018.
[12] R. J. van Sloun, O. Solomon, Y. C. Eldar, H. Wijkstra, and M. Mischi, "Sparsity-driven super-resolution in clinical contrast-enhanced ultrasound," in *Ultrasonics Symposium (IUS), 2017 IEEE International*. IEEE, 2017, pp. 1–4.
[13] A. Bar-Zion, O. Solomon, C. Tremblay-Darveau, D. Adam, and Y. C. Eldar, "Sparsity-based ultrasound super-resolution imaging," in *Proceedings of the 23rd European symposium on Ultrasound Contrast Imaging*, 2017, pp. 156–157.
[14] R. J. van Sloun, O. Solomon, M. Bruce, Z. Z. Khaing, H. Wijkstra, Y. C. Eldar, and M. Mischi, "Super-resolution ultrasound localization microscopy through deep learning," *arXiv preprint arXiv:1804.07661*, 2018.
[15] A. Bar-Zion, O. Solomon, C. Tremblay-Darveau, D. Adam, and Y. C. Eldar, "Sparsity-based ultrasound super-resolution hemodynamic imaging," *arXiv preprint arXiv:1712.00648*, 2017.
[16] N. Vaswani and W. Lu, "Modified-cs: Modifying compressive sensing for problems with partially known support," *IEEE Transactions on Signal Processing*, vol. 58, no. 9, pp. 4595–4607, 2010.
[17] N. Vaswani, "Kalman filtered compressed sensing," in *Image Processing, 2008. ICIP 2008. 15th IEEE International Conference on*. IEEE, 2008, pp. 893–896.
[18] D. Angelosante, S. I. Roumeliotis, and G. B. Giannakis, "Lasso-kalman smoother for tracking sparse signals," in *Signals, Systems and Computers, 2009 Conference Record of the Forty-Third Asilomar Conference on*. IEEE, 2009, pp. 181–185.
[19] D. Angelosante, G. B. Giannakis, and E. Grossi, "Compressed sensing of time-varying signals," in *Digital Signal Processing, 2009 16th International Conference on*. IEEE, 2009, pp. 1–8.
[20] A. Beck and M. Teboulle, "A Fast Iterative Shrinkage-Thresholding Algorithm for linear inverse problems," *SIAM Journal on Imaging Sciences*, vol. 2, no. 1, pp. 183–202, 2009.
[21] Y. C. Eldar and G. Kutyniok, *Compressed sensing: theory and applications*. Cambridge University Press, 2012.
[22] E. J. Candes, M. B. Wakin, and S. P. Boyd, "Enhancing sparsity by reweighted l_1 minimization," *Journal of Fourier analysis and applications*, vol. 14, no. 5-6, pp. 877–905, 2008.
[23] D. Reid, "An algorithm for tracking multiple targets," *IEEE transactions on Automatic Control*, vol. 24, no. 6, pp. 843–854, 1979.
[24] Y. Bar-Shalom and X.-R. Li, *Multitarget-multisensor tracking: principles and techniques*. YBs London, UK:, 1995, vol. 19.
[25] Y. Bar-Shalom, X. R. Li, and T. Kirubarajan, *Estimation with applications to tracking and navigation: theory algorithms and software*. John Wiley & Sons, 2004.
[26] J. L. Barron, D. J. Fleet, and S. S. Beauchemin, "Performance of optical flow techniques," *International journal of computer vision*, vol. 12, no. 1, pp. 43–77, 1994.
[27] M. Ovesnỳ, P. K**ríž**ek, J. Borkovec, Z. **S**vindrych, and G. M. Hagen, "Thunderstorm: a comprehensive imageJ plug-in for palm and storm data analysis and super-resolution imaging," *Bioinformatics*, vol. 30, no. 16, pp. 2389–2390, 2014.